Towards testing CMB anomalies using the kinetic and polarized Sunyaev-Zel'dovich effects

Juan I. Cayuso[1,2,*] and Matthew C. Johnson[1,3,†]

[1]*Perimeter Institute for Theoretical Physics, Waterloo, Ontario N2L 2Y5, Canada*
[2]*Department of Physics and Astronomy, University of Waterloo, Waterloo, Ontario, N2L 3G1, Canada*
[3]*Department of Physics and Astronomy, York University, Toronto, Ontario, M3J 1P3, Canada*

(Received 15 July 2019; accepted 27 May 2020; published 11 June 2020)

Measurements of the cosmic microwave background (CMB) temperature anisotropies on large angular scales have uncovered a number of anomalous features of marginal statistical significance, such as a hemispherical power asymmetry, a lack of power on large angular scales, and features in the power spectrum. Because the primary CMB temperature, the power spectrum has been measured at the cosmic variance limit; determining if these anomalies are hints of new physics as opposed to foregrounds, systematics, or simply statistical flukes requires new observables. In this paper, we highlight the potential contribution that future measurements of the kinetic Sunyaev-Zel'dovich effect (kSZ) and the polarized Sunyaev-Zel'dovich effect (pSZ) could make in determining the physical nature of several CMB anomalies. The kSZ and pSZ effects, temperature, and polarization anisotropies induced by scattering from free electrons in the reionized Universe are the dominant blackbody contribution to the CMB on small angular scales. Using the technique of SZ tomography, measurements of kSZ and pSZ effects can be combined with galaxy surveys to reconstruct the remote CMB dipole and quadrupole fields, providing a three-dimensional probe of large scale modes inside our Hubble volume. Building on previous work, we forecast the additional constraining power that these observables might offer for a representative set of anomaly models in the scenario of idealized next-generation CMB experiments and galaxy surveys. We find that the remote CMB dipole and quadrupole can yield constraints on anomalies models significantly beyond what can be done with CMB temperature and polarization on large scales, and comparable to what is possible with a large photometric galaxy survey. The best constraints are obtained from a multitracer analysis including the primary CMB, remote fields and galaxy survey.

DOI: 10.1103/PhysRevD.101.123508

I. INTRODUCTION

Anisotropies in the cosmic microwave background (CMB) are a powerful probe of early Universe physics. On large angular scales, these anisotropies encode primordial density fluctuations, which may ultimately have been produced at energy scales far beyond the reach of any terrestrial particle accelerator. Interestingly, a series of anomalous large angular scale features in the microwave sky have been reported by the WMAP and Planck [1,2] satellite missions, offering what could be hints of physics beyond the standard model of cosmology, ΛCDM (Λ cold dark matter). Several notable anomalies include: a hemispherical power asymmetry, a lack of correlations on large angular scales, features in the angular power spectrum, and an alignment of multipoles; see [3] for a recent review. As the statistical significance of each of these anomalies is rather modest, the most conservative position is to attribute them to statistical flukes, given the *a posteriori* nature of their discovery, systematics, or foregrounds. Unfortunately, as a stand-alone probe, the CMB temperature has already reached the limit imposed by cosmic variance on large angular scales, so new information can only come from alternative or complementary probes of the largest scales in the Universe.

Several observables have been identified as potential probes of physical models of the CMB anomalies, including CMB polarization (see, e.g., Refs. [4–11]), CMB lensing (see, e.g., [12,13]), the integrated Sachs-Wolfe (ISW) effect (see, e.g., [14–16]), and probes of large scale structure in the late Universe (see, e.g., [17–20]). Each of these observables has both advantages and disadvantages. CMB polarization can access scales comparable to those in the CMB temperature. On the largest angular scales, however, the mapping between the observed polarization anisotropies and physical scales is dependent on the (relatively poorly constrained) history of reionization. In addition, on large scales, galactic foregrounds are challenging (though not impossible) to remove [21]. The lensing potential can be reconstructed

*jcayuso@perimeterinstitute.ca
†mjohnson@perimeterinstitute.ca

with high fidelity using future CMB data sets (e.g., the Simons Observatory [22] or CMB-S4 [23]); however, there is limited support from the physical scales associated with many of the CMB anomalies (see [13]). If the (late time) ISW contribution to the CMB temperature can be isolated (e.g., using the technique of [16]), this could contribute a modest number of modes probing large scales. Finally, future galaxy surveys (e.g., LSST [24], Euclid [25], Spherex [26]) or 21 cm experiments (e.g., CHIME [27], HIRAX [28]; see also [29]) can reach large enough volumes to offer new information on some of the CMB anomalies. While promising the measurement of a huge number of modes on linear scales, there will be limited support on physical scales responsible for the lowest multipoles of the CMB temperature, and measurement of the largest modes will be noisy and plagued by various systematics (see, e.g., [30]).

The goal of this paper is to explore a new set of observables that may become important tools in the study of the physical nature of CMB anomalies: the remote dipole and quadrupole fields, i.e., the $\ell = 1$, 2 moments of the microwave sky measured throughout our observable Universe. The remote dipole manifests itself through the kinetic Sunyaev-Zel'dovich (kSZ) effect [31]: the dominant blackbody temperature contribution to *our* CMB sky on angular scales corresponding to multipoles $\ell \gtrsim 4000$ originates from free electrons on our past light cone scattering *their* locally observed CMB dipole. Similarly, in the presence of a local CMB quadrupole, the scattered photons are endowed with a polarization. The polarized component of the CMB arising after reionization, primarily from collapsed structures, is known as the polarized Sunyaev-Zel'dovich (pSZ) effect (as opposed to the component sourced near decoupling and at reionization, which is simply CMB polarization). The remote dipole and quadrupole can be reconstructed using the techniques of kinetic Sunyaev-Zel'dovich (kSZ) tomography [32–46] and polarized Sunyaev-Zel'dovich (pSZ) tomography [43,47–55]. Below, we refer to these two cases more generally as SZ tomography. In basic terms, this technique provides a three-dimensional reconstruction of the remote dipole and quadrupole fields by using the statistical anisotropy of the correlation between a tracer of LSS (e.g., a galaxy redshift survey) and the small-angular scale CMB temperature and polarization anisotropies. A set of quadratic estimators for the remote dipole and quadrupole fields were derived in Refs. [43,44,50], and a series of forecasts, including a demonstration with simulations in Ref. [56], has established detectability with future data sets [42–44,52].

Being primarily sensitive to inhomogeneities on large physical scales, these new observables that will become accessible with the next generation of CMB and galaxy surveys stand as potential candidates to further extend our understanding of the CMB anomalies. The remote quadrupole field receives support from the same scales contributing to the low-ℓ moments of the CMB temperature. Although at low redshift and on large angular scales, the remote quadrupole field is strongly correlated with the primary CMB temperature quadrupole [47,48]; there is significant new information on moderate angular scales and at high redshift [43,52,53,55]. The remote dipole field is dominated by the coarse-grained line-of-sight peculiar velocity field and is therefore sensitive to somewhat smaller scales than the remote quadrupole. However, it can be reconstructed at a far higher signal to noise and carries a significant amount of information on scales relevant to a variety of CMB anomalies. As general probes of physics on large scales, the remote dipole and quadrupole fields can yield improved constraints on primordial non-Gaussianity [45], primordial gravitational waves [50,55], and preinflationary relics [41].

The central question we wish to address in this work is whether or not the remote dipole and quadrupole fields could serve as alternative and complementary probes of the CMB anomalies to more traditionally considered tracers: the large scale E-mode CMB polarization and three-dimensional galaxy maps on our past light cone. An important fact to highlight is that measurements of these observables significantly differ in their nature: a key feature of SZ tomography is that it reconstructs large-scale inhomogeneities from anisotropies on the smallest angular scales. The fidelity of the reconstruction improves with the sensitivity and resolution of the CMB experiment and the depth and redshift errors of the galaxy survey. Therefore, the information accessible using SZ tomography will improve greatly with time, while direct probes of the largest scales are already close to the cosmic variance limit. Apart from offering an alternative way of measuring the large scale properties of the Universe, the remote dipole and quadrupole fields may also capture new independent information to that already available through the traditional probes.

Our methodology to estimate how informative the remote dipole and quadrupole fields could be for the study of the CMB anomalies consists of forecasting parameter constraints for physical models of the anomalies under the experimental conditions of idealized next-generation CMB experiments and galaxy surveys. We compare the performance of different combinations of the primary CMB temperature, CMB polarization, galaxy clustering, and the remote dipole and quadrupole fields. We assume that foreground-cleaned data are accessible for the CMB polarization on large scales, for the galaxy survey, and also for the kSZ and pSZ effects on small angular scales. The limiting experimental factors that we do take into account are CMB noise levels as expected for stage-4 CMB experiments and LSST like specifications for the galaxy survey, as well as calibration errors on large scales for the latter. We perform our forecast using a Fisher matrix formalism on a series of physical models for three representative CMB anomalies: the power asymmetry, the lack of power on large angular

scales, and a feature in the temperature power spectrum at multipoles around $\ell \sim 20$–30.

The plan of the paper is as follows. In Sec. II, we review SZ tomography and describe the properties of the remote dipole and quadrupole fields. In Sec. III, we describe the details of our forecast and introduce a figure of merit which is used to quantify the potential constraining power with different combinations of observables. In Sec. IV, we present the results of our forecast, and we conclude in Sec. V.

II. SZ TOMOGRAPHY: RECONSTRUCTING THE REMOTE DIPOLE AND QUADRUPOLE FIELDS

SZ tomography allows us to reconstruct the line-of-sight components of the CMB dipole and quadrupole moments as observed by free electrons on our past light cone. Here, we review the basic features of SZ tomography and the remote dipole/quadrupole fields; further details can be found in Refs. [43,44,56]. Contributions to the CMB temperature and polarization generated via the kinetic and polarized SZ effects can be expressed through the line of sight integrals,

$$\left.\frac{\Delta T}{T}\right|_{\rm kSZ}(\hat{\mathbf{n}}_e) = \int d\chi_e \dot{\tau}(\hat{\mathbf{n}}_e,\chi_e) v_{\rm eff}(\hat{\mathbf{n}}_e,\chi_e),$$
$$v_{\rm eff}(\hat{\mathbf{n}}_e,\chi_e) \equiv \sum_{m=-1}^{1} \Theta_1^m(\hat{\mathbf{n}}_e,\chi_e) Y_{1m}(\hat{\mathbf{n}}_e) \quad (1)$$

$$(Q \pm iU)^{\rm pSZ}(\hat{\mathbf{n}}_e) = \frac{\sqrt{6}}{10} \int d\chi_e \dot{\tau}(\hat{\mathbf{n}}_e,\chi_e) q^{\pm}_{\rm eff}(\hat{\mathbf{n}}_e,\chi_e),$$
$$q^{\pm}_{\rm eff}(\hat{\mathbf{n}}_e,\chi_e) \equiv \sum_{m=-2}^{2} \Theta_2^m(\hat{\mathbf{n}}_e,\chi_e) \mp_2 Y_{2m}(\hat{\mathbf{n}}_e), \quad (2)$$

where $\hat{\mathbf{n}}_e$ denotes the line of sight direction, χ_e the comoving distance to the scatterer, $\Theta_\ell^m(\hat{\mathbf{n}}_e,\chi_e)$ are the moments of the CMB temperature at the scatterer, and $\dot{\tau}(\hat{\mathbf{n}}_e,\chi_e)$ is the differential optical depth defined as

$$\dot{\tau}(\hat{\mathbf{n}}_e,\chi_e) \equiv -\sigma_T a(\chi_e) \bar{n}_e(\chi_e)[1+\delta_e(\hat{\mathbf{n}}_e,\chi_e)], \quad (3)$$

with $a_e(\chi_e)$ the scale factor, σ_T the Thompson cross section, and $\delta_e(\hat{\mathbf{n}}_e,\chi_e)$ the perturbations about the average electron number density $\bar{n}_e(\chi_e)$.

Figure 1 depicts the basic spacetime geometry of the SZ effect. The remote dipole field $v_{\rm eff}(\hat{\mathbf{n}}_e,\chi_e)$ is a projection of the CMB dipole $\Theta_1^m(\hat{\mathbf{n}}_e,\chi_e)$ as observed along the past light cone. The dominant contribution is from the line-of-sight component of the peculiar velocity field (as it is for our own observed CMB dipole), although there are subdominant contributions that come from the Sachs-Wolfe (SW), integrated Sachs-Wolfe (ISW), and primordial Doppler (velocities of the plasma at last-scattering) effects. These dominant and subdominant contributions are often referred

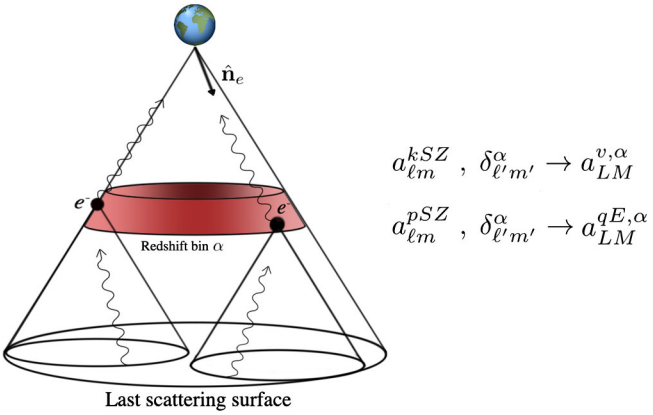

FIG. 1. Photons traveling from the last scattering surface can be rescattered by free electrons once the Universe is reionized. The small scale CMB signal generated through this process can be combined with a redshift dependent tracer of the electron density to reconstruct the moments $a^{v,\alpha}_{LM}$ and $a^{qE,\alpha}_{LM}$ of the dipole and quadrupole field.

in the literature as the kinematic and intrinsic CMB dipole, respectively. The remote quadrupole field $q^{\pm}_{\rm eff}(\hat{\mathbf{n}}_e,\chi_e)$ is a projection of the CMB quadrupole $\Theta_2^m(\hat{\mathbf{n}}_e,\chi_e)$ as observed along the past light cone. The remote quadrupole receives contributions from both scalar and tensor fluctuations, although we consider only scalar modes in the present context. In this case, $q^{+}_{\rm eff} = q^{-}_{\rm eff}$, and the remote quadrupole is curlfree. As such, we will denote the pure scalar remote quadrupole field as "qE". The remote quadrupole is sourced by the SW, ISW, and primordial Doppler effects. For further description of the contributions to the remote dipole and quadrupole fields, we refer the reader to Refs. [41–43,52,55,57].

SZ tomography works by first inferring the fluctuations in the optical depth in a set of redshift bins labeled by α from a tracer of structure such as a galaxy survey. A quadratic estimator for the bin-averaged dipole and quadrupole fields is then constructed from the CMB temperature or polarization and each redshift bin of the galaxy survey. We work in harmonic space for the reconstructed fields, denoting the moments of the dipole or quadrupole fields in each bin as $a^{v,\alpha}_{LM}$ and $a^{qE,\alpha}_{LM}$, respectively. The reconstruction noise on the remote dipole and quadrupole fields depends on the specifications of the CMB experiment and the volume and shot noise of the galaxy survey. We discuss our assumptions for the reconstruction noise in detail in the following section, which corresponds to the choices made in Ref. [43]. An additional consideration is the so-called "optical depth degeneracy" (see, e.g., [51,58]), which is a consequence of the necessarily imperfect inference of the fluctuations in the optical depth from the galaxy survey. This manifests itself as an overall multiplicative bias on the remote dipole and quadrupole fields in each redshift bin that must be marginalized over [44]. Direct measurements

of the distribution of free electrons, for example, using fast radio bursts as proposed in Ref. [59], can mitigate the optical depth degeneracy.

The remote dipole and quadrupole fields provide new information about the Universe on large scales. The primary CMB photons, traveling to us directly from the last scattering surface, probe the largest accessible scales. The information they provide, however, is somewhat obscured due to the fact that we observe the projection of three-dimensional inhomogeneities onto a two-dimensional surface. As illustrated in Fig. 1, the remote dipole and quadrupole fields accessed through SZ tomography provide additional information in a number of ways. First, due to the tomographic nature of the reconstruction, we obtain coarse-grained three-dimensional information. Furthermore, the remote dipole and quadrupole fields are sensitive to inhomogeneities *inside our past light cone*, implying that they can access *different* information than what is encoded in the primary CMB temperature. In the case of the remote dipole field, which is dominated by the local peculiar velocity, it is possible to study bulk motion on scales comparable to the size of the observable Universe using long-range correlations.

To go beyond these qualitative remarks, we inspect the scales probed by the remote dipole and quadrupole fields using linear theory, which is a good approximation for the scales under consideration. The various observables under consideration can be related to primordial gravitational potential in Newtonian gauge $\Psi_i(\boldsymbol{k})$ using a set of (bin-averaged) transfer functions $\Delta_\ell^{X,\alpha}(k)$,

$$a_{\ell m}^{X,\alpha} = \int \frac{d^3\boldsymbol{k}}{(2\pi)^3} \Delta_\ell^{X,\alpha}(k) \Psi_i(\boldsymbol{k}) Y_{lm}^*(\hat{\boldsymbol{k}}), \tag{4}$$

where $X = T, E, v, qE, G$ for the observables we consider in this work (primary CMB temperature, E-mode polarization, remote dipole, remote quadrupole, and redshift galaxy distribution, respectively); for $X = T$, E, the index α is superfluous. Expressions for the remote dipole and quadrupole transfer functions, which capture the contributions coming from the SW, ISW, and Doppler effects, can be found in [60,61].

The transfer functions reveal to us which scales the remote dipole and quadrupole are sensitive to. As an example, we show in Fig. 2 the ΛCDM transfer functions (e.g., using parameters from Planck 2018 [21]) in the (ℓ, k) plane for the primary CMB temperature, E-mode polarization and the remote fields at a few different redshifts. For the CMB temperature and remote dipole field, we plot the range $1 \leq \ell \leq 30$, which roughly encompasses the range of scales relevant to the CMB anomalies we consider. For the CMB E-mode polarization and remote quadrupole, we restrict the range to $1 \leq \ell \leq 10$, as this is the range over which the remote quadrupole receives significant support. There are a few things to note from this figure. Comparing with the CMB temperature transfer function, we see that the remote dipole and quadrupole fields have good support over a comparable range of wave numbers. Because it is sourced mostly by fluctuations near the time of last scattering, the remote quadrupole is relatively more sensitive to large scales than the remote dipole. However, the amplitude of the remote quadrupole falls sharply with ℓ, implying (correctly) that there will be a limited number of measurable modes. It can also be noted that the remote dipole field probes larger scales at higher redshift; this is due to the larger physical distances in the peculiar velocity field which are sampled.

Based on these observations, the observables returned by SZ tomography appear to have the potential to add statistical power into the analysis of CMB anomalies due to their sensitivity to large scale inhomogeneities. However, the amount of *new* information that can be added will depend on the correlations that exist amongst all the observables we consider. Indeed, some correlations are expected to be there by construction. For example, at low redshift, the $\ell = 2$ moments of the remote quadrupole field are perfectly correlated with the CMB temperature quadrupole [47,48,52].

In Fig. 3, we plot the correlation coefficient between the remote fields and the primary CMB, defined by

$$r_{\alpha\beta,\ell\ell',mm'}^{X,Y} = \frac{C_{\alpha\beta,\ell\ell',mm'}^{X,Y}}{\sqrt{C_{\alpha\alpha,\ell\ell,mm}^{X,X} C_{\beta\beta,\ell'\ell',m'm'}^{Y,Y}}}, \tag{5}$$

where

$$C_{\alpha\beta,\ell\ell',mm'}^{X,Y} = \int \frac{d^3\boldsymbol{k}}{(2\pi)^3} \int \frac{d^3\boldsymbol{k}'}{(2\pi)^3} \Delta_\ell^{*X,\alpha}(k) \Delta_{\ell'}^{Y,\beta}(k') \times \langle \Psi_i^*(\vec{\boldsymbol{k}}) \Psi_i(\vec{\boldsymbol{k}'}) \rangle Y_{\ell m}(\hat{\boldsymbol{k}}) Y_{\ell' m'}^*(\hat{\boldsymbol{k}}') \tag{6}$$

are the elements of the covariance matrix. In the top panel, we show the correlations between the CMB temperature and remote fields at a few values of ℓ. For $\ell = 1$, the CMB temperature is the aberration-free dipole (see, e.g., Refs. [62–65] for a summary of the various frames for the CMB dipole), not the dipole observed in the Earth's rest frame. There is $\lesssim$10%–20% correlation between the CMB temperature and the remote dipole field over a range of redshifts and multipoles. There is a far higher correlation between the CMB temperature and the remote quadrupole field. As expected, there is a nearly perfect correlation between the CMB quadrupole and the $\ell = 2$ moment of the remote quadrupole field, except at the highest redshifts. The remote dipole field has little correlation with the CMB E-mode polarization. However, at the highest redshift, there is a near-perfect correlation between the E-mode polarization and the remote quadrupole field. This is expected, since at high redshift, the CMB polarization is sourced by the same remote quadrupole field that is being

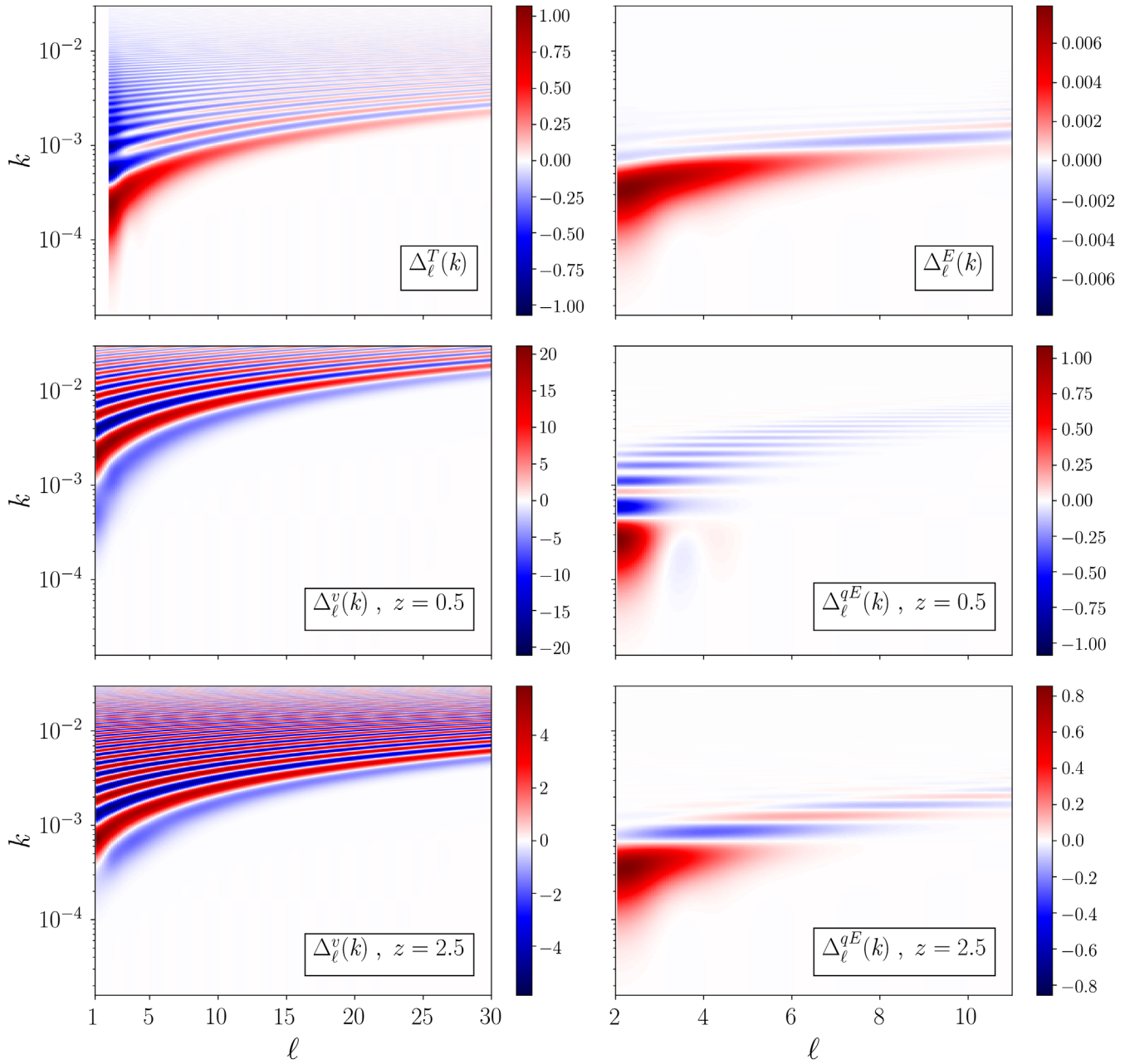

FIG. 2. On the top panels, the transfer functions for the primary CMB temperature ($\ell = 1$ is not plotted here) and E-mode polarization. On the middle and bottom, the bin averaged transfer functions for the remote dipole (left) and quadrupole (right) for bins centered on redshifts $z = 0.1$ and $z = 2.5$. The binning scheme used for this figure consisted on 60 bins of equal comoving size between $0.1 \leq z \leq 6$.

reconstructed by SZ tomography (see Ref. [55] for further discussion). Significant correlations will also exist between the galaxy redshift distribution and the reconstructed dipole field, as the latter is dominated by the line of sight peculiar velocity field, which certainly has a tight relationship with the density field itself.

In conclusion, including the full covariance between the various observables can be important in a joint analysis, such as the one we present below. This is particularly important at low-multipoles/low-redshift for the CMB temperature, at high-redshift for the CMB E-mode polarization, and in general, for the galaxy-velocity correlations. Conversely, we see that over a wide range of multipoles and redshifts, the remote dipole and quadrupole fields carry significant independent information beyond the primary CMB temperature and polarization. For the case of the remote dipole, velocities are sensitive to the gradient of the gravitational potential and thus, can probe inhomogeneities on slightly larger scales than the directly observed densities.

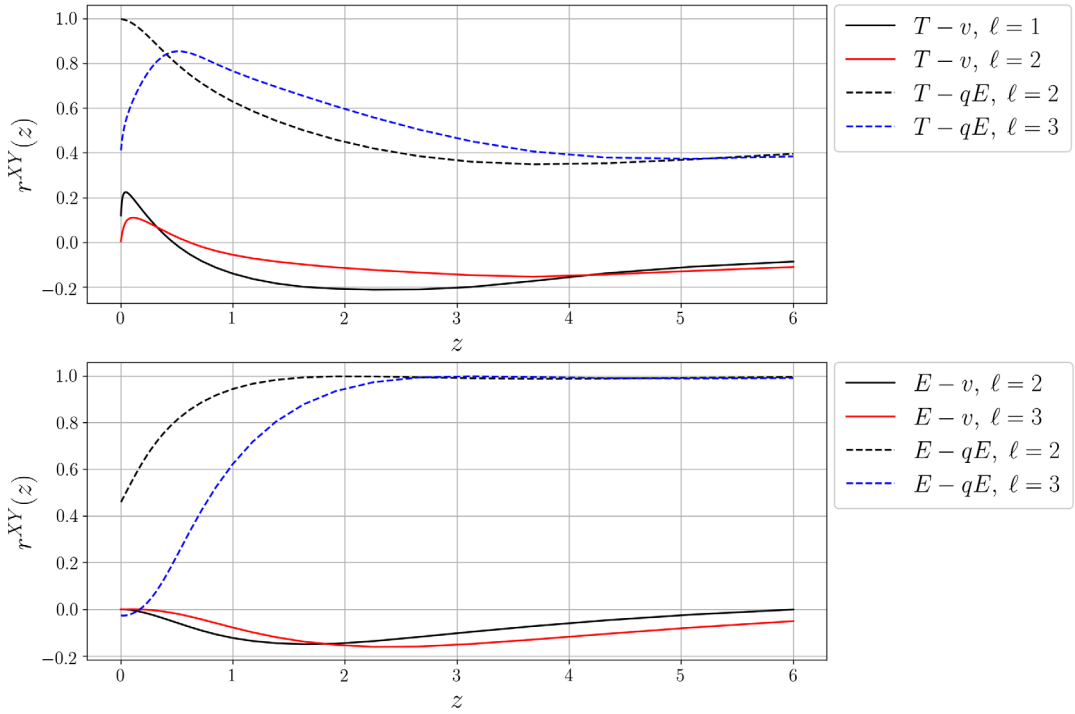

FIG. 3. Correlation coefficient between the primary CMB fields and the remote dipole an quadrupole fields. As expected, the $\ell = 2$ moment of the primary CMB temperature is perfectly correlated with the very low redshift remote quadrupole (top panel, black dashed line) and the remote dipole captures the primordial contributions to the $\ell = 1$ aberration-free CMB dipole measured at $z = 0$ (top panel, black solid line). The remote quadrupole exhibits longer range correlations with the primary CMB than the remote dipole does (bottom panel).

III. FORECAST SETUP

The reconstruction of the remote dipole and quadrupole fields using SZ tomography opens the possibility of bringing new information into the study of the large scale CMB anomalies. Determining how informative a data set is will depend, of course, on the type of questions we are trying to answer. From the Bayesian perspective, we might strive for model selection: how would adding a new observable change the odds ratio between the anomaly model and ΛCDM in a future experiment (see, e.g., [66])? Such an approach requires a motivated set of theoretical priors, as well as an understanding of the full likelihood function over model parameters. Due to the lack of strongly motivated models and the computational complexity of evaluating the full likelihood function, we do not pursue this approach here. Another possibility (less computationally expensive than model selection) for predicting how informative a data set can be is to determine its constraining power on the parameters of a model using a Fisher matrix-based approach. In general, such results are not sufficient to decide if a future experiment could choose among competing theoretical models. However, this approach does offer a way of quantifying the additional constraining power a new observable might add. We will adopt this methodology in order to study the information content of the remote dipole and quadrupole field on a series of models for CMB anomalies and compare it to what is achievable using the primary CMB temperature, E-mode polarization, and galaxy clustering on large angular scales. We now proceed to describe our definitions for information content and modeling for the signal and noise covariance.

A. Fisher analysis, figure of merit, and parameter space

Given a cosmological model with parameters $\{\lambda_i\}$, one can forecast how well these parameters can be constrained using a different set of observables by implementing a Fisher matrix analysis. The elements of the Fisher matrix are given by the following expression:

$$\mathbf{F}_{ij} = \frac{1}{2}\mathrm{Tr}[(\mathbf{C}+\mathbf{N})^{-1}\mathbf{C}_{,\lambda_i}(\mathbf{C}+\mathbf{N})^{-1}\mathbf{C}_{,\lambda_j}], \tag{7}$$

where $\mathbf{C}$ is the signal covariance matrix [whose elements are defined by Eq. (6)], $\mathbf{C}_{,\lambda_j}$ denotes its derivative respect to λ_j, and $\mathbf{N}$ is the noise covariance matrix. The Fisher matrix encodes information about the curvature of the likelihood function around its maximum in parameter space, and this information can be turned into fully marginalized constraints on the model parameters,

$$\sigma_{\lambda i} = \sqrt{(\mathbf{F}^{-1})_{ii}}. \tag{8}$$

A good way of comparing the results of the Fisher matrix analysis among models with a different number of parameters is to define a single quantity that condenses the information of how well the model parameters are constrained. For a forecast using a set $\{X\}$ of observables, we define the figure of merit (FoM) for a subset of N parameters,

$$\mathrm{FoM}(X) = \left(\frac{1}{\sqrt{\det(\mathbf{F_N^{-1}})}}\right)^{\frac{1}{N}}, \tag{9}$$

where $\mathbf{F_N^{-1}}$ is the part of the inverse Fisher matrix containing information about the fully marginalized constraints on the subset of parameters. Furthermore, since we want to highlight the relative performance respect to the primary CMB, we will express our results in terms of a figure of merit ratio, defined by

$$\mathrm{FoMr}(X) = \frac{\mathrm{FoM}(X)}{\mathrm{FoM}(T)}. \tag{10}$$

The figure of merit ratio encodes the geometrical mean improvement on model parameter constraints. Similar figure of merit ratios have been used in previous literature, e.g., as a measure of improvement in constraints on CMB anomalies parameters when comparing current to future missions [67].

Apart from the standard ΛCDM parameters and the extra parameters a_i present in any of its extensions, it is important to marginalize over other "nuisance" parameters that can be introduced depending on our set of observables $\{X\}$. For the case of the remote fields, we need to include a bias parameter b_α^d multiplying the multipole coefficients $a_{LM}^{v,\alpha}$ and $a_{LM}^{qE,\alpha}$ in each bin α due to the optical depth degeneracy in kSZ/pSZ: having incomplete inference of the electron-galaxy cross spectrum, we can only reconstruct the remote dipole and quadrupole inside each redshift bin up to an overall amplitude. We refer the reader to [44] for a more detailed discussion of the optical depth degeneracy. Modeling of galaxy clustering also involves the introduction of other nuisance parameters: galaxies are biased tracers of the dark matter distribution, so its necessary to include a galaxy bias $b^G(z)$, which will depend on the details of the galaxy survey and can also be marginalized over. On large scales, there are as well contributions to the observed galaxy number counts which come from redshift spatial distortions, lensing, and GR effects on very large scales. These contributions have their own internal biases (intrinsic alignment bias, evolution bias, magnification bias) for which we provide references in the following section. The fiducial values for the ΛCDM cosmology we take are $\Omega_b = 0.049$, $\Omega_c = 0.263$, $h = 0.675$, $\tau = 0.054$, $10^9 A_s = 2.096$, and $n_s = 0.965$. Fiducial values for each of the anomalies model parameters are presented together with the models in the next section and the Appendix A. The bias parameters b_α^d are assigned fiducial values of unity. Priors on b_α^d can come from other astrophysical probes [59], but for the anomaly models under consideration, we find that the constraints are relatively insensitive to the addition of such a prior. Parameters b_α^G are obtained by averaging the galaxy bias $b^G(z)$ over the survey redshift bins. The fiducial values we use for this bias are $b^G(z) \simeq 0.95 + 0.67z$ as quoted in the LSST science book [24].

B. Modeling of the signal

The signal covariance matrix $\mathbf{C}$ we construct is split into two pieces: $\mathbf{C}^{\mathrm{low}}$ and $\mathbf{C}^{\mathrm{high}}$. For multipoles $\ell \leq 60$, corresponding to $\mathbf{C}^{\mathrm{low}}$, we investigate different combinations of all observables under consideration, accounting for the auto and cross-correlations between the primary CMB temperature and E-mode polarization, remote dipole/quadrupole fields and galaxy number counts. For multipoles $60 < \ell < \ell_{\mathrm{high}}$, where the reconstruction of the remote dipole and quadrupole fields is poor, and where correlations with the primary CMB are vanishingly small, we include only the CMB temperature and polarization (and their covariance) in $\mathbf{C}^{\mathrm{high}}$. We choose $\ell_{\mathrm{high}} = 3000$ since for higher multipoles the primary CMB becomes a subdominant contribution to the measured microwave sky. With these assumptions, the Fisher matrix factorizes into the sum of a low-ℓ and high-ℓ piece, $\mathbf{F}^{\mathrm{low}}$ and $\mathbf{F}^{\mathrm{high}}$, respectively. The main effect of $\mathbf{F}^{\mathrm{high}}$ is to constrain the ΛCDM parameters. We further assume that $\mathbf{F}^{\mathrm{high}}$ is zero for the entries corresponding to the anomaly model parameters a_i, since the anomaly models under consideration will have little to no effect on these scales. The elements of the covariance matrix are computed using Eq. (6). We obtain the primary CMB temperature and polarization transfer functions using the publicly available code for anisotropies in the microwave background (CAMB) [68]. We use the same conventions and definitions for the remote fields transfer functions as in [43] (Appendixes A and C), and for the galaxy number counts, we follow what is done in related work [69] (Appendix A), where dipole reconstruction is put together with galaxy number counts to determine if large scale general relativistic effects could be detected with near future surveys.

C. Modeling of the noise

The noise covariance matrices for the primary CMB fields and for galaxy number counts are constructed under the assumption of idealized next generation CMB experiments and galaxy surveys. We assume CMB temperature and polarization data on the full sky with noise

$$\mathbf{N}_\ell^{\rm CMB} = \eta^2 \exp\left(\frac{\theta^2_{\rm FWHM}}{8\log 2}\ell(\ell+1)\right). \tag{11}$$

We choose fiducial values of $\eta = 1\ \mu K$-arcmin and $\theta_{\rm FWHM} = 1$ arcmin, representative of stage-4 CMB-like experiments, and explore how constraints vary for larger (5 μK-arcmin), smaller (0.1 μK-arcmin) noise and increased beam size ($\theta_{\rm FWHM} = 5$ arcmin). To determine the galaxy survey shot noise, we assume an LSST-like number density per arc-minute square given by

$$n(z) = n_{\rm gal}\frac{1}{2z_0}\left(\frac{z}{z_0}\right)^2 \exp\left(-z/z_0\right), \tag{12}$$

where $z_0 = 0.3$ and $n_{\rm gal} = 40$ arcmin^{-2}. In addition to the shot noise, we also account for photometric calibration errors, which introduce additional biases to the large galaxy power spectrum, and we base our parametrization on previous studies on the impact of these systematics in the reconstruction of the ISW effect from galaxy surveys [70,71]. Calibration errors introduce extra power $C_\ell^{\rm cal}$, which can be modeled by

$$C_\ell^{\rm cal} = A_{\rm cal} e^{-(\ell/10)^2} \tag{13}$$

for multipoles $\ell < 30$ and zero otherwise, where $A_{\rm cal}$ is a normalization constant chosen such that the variance of the calibration error field defined on the sky is equal to a desired value. We choose this variance to be equal to 10^{-4}, which corresponds to a level of calibration of $\approx$0.01 magnitudes and is a rather conservative value for what is expected from future surveys. We do not marginalize over the calibration error parameters.

For the remote fields, the reconstruction noise is computed as in Ref. [43]. The instrumental CMB noise discussed above is one of the necessary pieces to calculate the reconstruction noise for the dipole and quadrupole correlations appearing in $\mathbf{C}^{\rm low}$. Multipoles up to $\ell = 9000$ (assumed to be accessible with next generation experiments) are used to calculate the reconstruction noise, and thus, different choices of the CMB noise level η and beam size $\theta_{\rm FWHM}$ will have an impact on the signal to noise for the low-ℓ dipole and quadrupole fields. The galaxy shot noise enters into the calculation in a similar way, but we have kept the parameters appearing in Eq. (12) fixed in order to focus on improvements on constraints due to the reconstructed fields and their dependence on CMB noise parameters.

The construction of both the signal and noise covariance matrices also involves a choice of redshift binning for the galaxy survey, which determines how coarse-grained the reconstructed remote dipole and quadrupole fields are. The thinner the binning is, the more information can be collected. Clearly, all independent information would be captured in the limit of having infinitely small redshift bins, but the redshift resolution of the (photometric redshift) surveys used in the reconstruction process imposes a limit on how many redshift bins can be used. We use 45 redshift bins of equal comoving radial width between $Z = [0.1, 3]$, which, translating to redshfit, is roughly consistent with the expected photometric redshift errors for LSST [24].

IV. INFORMATION CONTENT FORECAST

In what follows, we present the Fisher forecast for constraints on models of the large scale CMB anomalies using different subsets of observables: $X = (T, E)$, $X = (T, E, R)$, $X = (T, E, G)$, and $X = (T, E, R, G)$. We first introduce two general classes of physical models: models that break statistical isotropy, which could be responsible for the power asymmetry, and models that deviate from a nearly scale-invariant primordial power spectrum, which could be responsible for a lack of power on large scales and a feature in the power spectrum at $\ell \sim 20$–30. While this is a small subset of physical models considered to explain only a subset of the CMB anomalies, we hope that the cases we do consider are illustrative of the potential utility of SZ tomography for providing further insight into the nature of the CMB anomalies. Following this, we present the figure of merit ratio FoMr given by Eq. (10) for each model, which provides a quantitative measure of the overall improvement on parameter constraints relative to what is achievable with measurements of the primary CMB temperature only. The fully marginalized parameter constraints for each model can be found in Appendix A.

A. Statistical isotropy breaking

A subset of the observed CMB anomalies suggests the existence of statistical anisotropies [72]: unexpected alignment between the low multipole moments, a hemispherical power asymmetry, parity asymmetry of the CMB etc. It is still not known whether or not these features are due to foregrounds, local cosmic structure, or possible statistical flukes present in our observed realization of ΛCDM. However, if due to true physical departures from ΛCDM, the underlying model must break statistical isotropy.

We consider phenomenological models of spontaneous isotropy breaking [73] (see also, e.g., [74–77]), in which local observers would detect statistical anisotropy, while the Universe as a whole is globally, statistically homogeneous and isotropic. Following Ref. [4], we include a field $h(\vec{x})$ with super horizon fluctuations that modulates the potential $g_1(\vec{x})$ only on large scales, leaving small scale fluctuations described by $g_2(\vec{x})$ unaffected

$$\Psi_i(\vec{x}) = g_1(\vec{x})(1 + h(\vec{x})) + g_2(\vec{x}). \tag{14}$$

Here, $g_1(\vec{x})$ and $g_2(\vec{x})$ are random Gaussian fields, while $h(\vec{x})$ is deterministic within our Hubble volume. It is the

slow variation of $h(\vec{x})$ inside our Hubble volume that is responsible for the existence of statistical anisotropy in the CMB. Such a modulation can occur, for example, in inflation models with more than one field contributing to the primordial curvature perturbations. Here, rather than focusing in a particular early Universe mechanism for generating the modulation, we are interested in determining how the imprints of a preferred direction on the remote dipole and quadrupole fields can help to constrain the amplitude of the modulation.

The effect on the primordial power spectrum is given by

$$\begin{aligned}\langle \Psi_i^*(\vec{k})\Psi_i(\vec{k'})\rangle &= (2\pi)^3\delta(\vec{k}-\vec{k'})(P_{g_1}(k)+P_{g_2}(k')) \\ &+ (P_{g_1}(k)+P_{g_1}(k'))h(\vec{k}-\vec{k'}) \\ &+ \int \frac{d^3\tilde{k}}{(2\pi)^3}P_{g_1}(\tilde{k})h(\vec{k}-\vec{\tilde{k}})h(\vec{k'}-\vec{\tilde{k}}), \end{aligned} \quad (15)$$

where $P_{g_1}(k)$ and $P_{g_2}(k)$ are the power spectra for $g_1(\vec{x})$ and $g_2(\vec{x})$. We will fix these power spectra to that $P_{g_1}(k)+P_{g_2}(k)=P_{\Lambda\mathrm{CDM}}(k)$, when $h(\vec{x})=0$. The second and third term will induce couplings between different (ℓ, m) multipoles, and this manifests the breaking of statistical isotropy for local observers.

For this work, consider a dipolar modulation given by a superhorizon scale mode varying in the direction of the z axis,

$$h(\vec{x}) = A\frac{\sin(\vec{k}_0\cdot\vec{x})}{k_0\chi_{\mathrm{dec}}} \approx A\frac{z}{\chi_{\mathrm{dec}}}. \quad (16)$$

This physical model could explain the observed power asymmetry [4] (see also, e.g., [9,13,78]); we do not consider other modulation models here, which could be responsible for the observed alignment of low-ℓ multipoles (see, e.g., [4]) or other observed CMB anomalies. For the modulating field Eq. (16), expressions for elements of the covariance matrix up to second order in A can be obtained analytically and are presented in Appendix B. Analysis of temperature data by Planck [72] suggests a phenomenological dipole modulation up to $\ell \sim 60$ with a value for the amplitude parameter of approximately [72] $A = 0.07 \pm 0.02$. An open question is to what scales the asymmetry might persist, e.g., where the crossover occurs from the observed fluctuations being sourced by g_1 to being sourced by g_2. There is a hard upper bound implied by the low hemispherical asymmetry of the distribution of high redshift quasars [79] of $k \lesssim 1$ Mpc^{-1}. In the following, we treat the crossover to statistical homogeneity as in Ref. [13], where a new set of parameters describing the crossover is introduced,

$$P_{g_1}(k) = \frac{1}{2}P_{\Lambda\mathrm{CDM}}(k)\left[1-\tanh\left(\frac{\ln k-\ln k_c}{\Delta\ln k}\right)\right], \quad (17)$$

with k_c a cutoff scale with fiducial value 7.83×10^{-3} Mpc^{-1} and $\Delta\ln k = 0.5$ a parameter controlling the steepness of the crossover.

B. Deviations from ΛCDM power law

The other class of models we consider involves possible deviations from the ΛCDM power law primordial power spectrum. On large angular scales, it has been observed by WMAP and Planck that the CMB temperature shows an unexpected lack of variance compared to ΛCDM. Features in the temperature power spectrum have also been identified, remarkable ones being a low quadrupole and a lack of power at multipoles $\ell \sim 20$–30. One simple and theoretically interesting possibility is that these CMB anomalies are due to corresponding features in the primordial power spectrum of curvature fluctuations. Such features can arise as a signature of: the onset of inflation (e.g., [80–82]), oscillations [83,84] or sharp steps [85] in the inflaton potential, steps in the sound speed [86], or DBI inflation warp factor [87], among other scenarios. In this section, we determine the additional constraining power offered by SZ tomography for a subset of these feature models, choosing a few representative examples that have previously been investigated by Planck [88].

1. Phenomenological models for large scale power suppression

Following Ref. [88], we consider a set of two-parameter phenomenological models for the suppression of power on large angular scales in the primary CMB temperature. The first model we consider [82] implements an exponential suppression of power below a wave number k_c,

$$P_{s_1}(k) = P_{\Lambda\mathrm{CDM}}(k)\left(1-\exp\left[-\left(\frac{k}{k_c}\right)^{\lambda}\right]\right), \quad (18)$$

where $P_{\Lambda\mathrm{CDM}}(k) = A_s(\frac{k}{k_*})^{n_s-1}$ and the best-fit model parameters from Planck 2015 [88] are $k_c = 3.74\times10^{-4}$ Mpc^{-1} and $\lambda = 0.53$. The second model has a break in the power law at a scale k_b,

$$P_{s_2}(k) = \begin{cases} A_s\left(\frac{k_b}{k_*}\right)^{-\delta}\left(\frac{k}{k_*}\right)^{n_s-1+\delta} & \text{if } k \le k_b, \\ A_s\left(\frac{k}{k_*}\right)^{n_s-1} & \text{if } k \ge k_b. \end{cases} \quad (19)$$

The best-fit model parameters from Planck 2015 [88] are $k_b = 5.26\times10^{-4}$ Mpc^{-1} and $\delta = 1.14$. In both cases, we choose the central values for the model parameters as the best-fit Planck values, and we fix the pivot scale to $k_* = 0.05$ Mpc^{-1}. We plot the two fiducial models in Fig. 4.

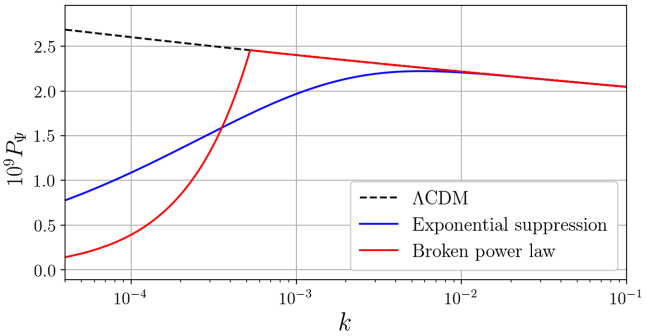

FIG. 4. Primordial power spectrum for the exponential suppression model and the broken power law model together with the standard ΛCDM spectrum. The first model shows suppression starting at scales of several hundred Mpc, while the second one deviates from the standard power law on scales of several Gpc.

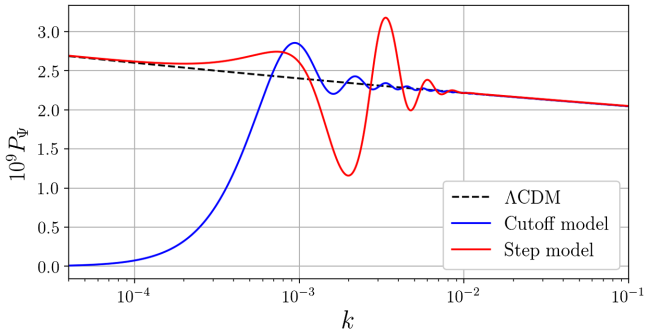

FIG. 5. Primordial power spectrum for the cutoff model and the step model together with the standard ΛCDM spectrum.

2. Features in the power spectrum

We now review two physical scenarios that give rise to features in the primordial power spectrum. In the first model, we consider a period of kinetic domination preceding slow-roll inflation. This gives rise to a suppression of power on large scales, as well as oscillations in the power spectrum on intermediate scales [82]. The one parameter in this model is a scale k_c, roughly corresponding to the comoving size of the horizon when slow-roll begins. Clearly, we are able to constrain this model only when there are a minimal number of e-folds of inflation, in which case k_c is on observable scales. The full form of the power spectrum is given by

$$\ln P_c(k) = \ln P_0(k) + \ln\left(\frac{\pi}{16}\frac{k}{k_c}|C_c - D_c|^2\right), \tag{20}$$

where

$$C_c = \exp\left(\frac{-ik}{k_c}\right)\left[H_0^{(2)}\left(\frac{k}{2k_c}\right) - \left(\frac{k_c}{k}+i\right)H_1^{(2)}\left(\frac{k}{2k_c}\right)\right],$$
$$D_c = \exp\left(\frac{ik}{k_c}\right)\left[H_0^{(2)}\left(\frac{k}{2k_c}\right) - \left(\frac{k_c}{k}-i\right)H_1^{(2)}\left(\frac{k}{2k_c}\right)\right], \tag{21}$$

and $H_n^{(2)}$ denotes the Hankel function of the second kind. We assume the best-fit value from Planck 2015 [88] of $k_c = 3.63 \times 10^{-4}$ Mpc^{-1} as the central values in our analysis below. The second model we consider arises when there is a tanh-shaped step in the inflaton potential as in Ref. [89], which gives rise to oscillations in the primordial power spectrum. This is a three-parameter model, which, at the level of the inflaton potential, corresponds to the location, height, and width of the step. The resulting power spectrum is given by

$$\ln P_s(k) = \exp\left[\ln P_0(k) + I_0(k) + \ln\left(1 + I_1^2(k)\right)\right], \tag{22}$$

where

$$I_0(k) = \frac{\mathcal{A}_s}{2x^3}\left[(18x - 6x^3)\cos 2x + (15x^2 - 9)\sin 2x\right]\Big|_{x=(k/k_s)} \times \mathcal{D}\left(\frac{k/k_s}{x_s}\right) \tag{23}$$

$$I_1(k) = \frac{1}{\sqrt{2}}\left[\frac{\pi}{2}(1-n_s) - \frac{\mathcal{A}_s}{x^3}\{3(x\cos x - \sin x) \times [3x\cos x + (2x^2-3)\sin x]\}\Big|_{x=(k/k_s)} \times \mathcal{D}\left(\frac{k/k_s}{x_s}\right)\right]. \tag{24}$$

$$\mathcal{D}(x) = \frac{x}{\sinh x} \tag{25}$$

We assume the best-fit value from Planck 2015 [88] of $\mathcal{A}_s = 0.374$, $k_s = 7.94 \times 10^{-4}$ Mpc^{-1}, and $x_s = 1.41$. We plot the power spectra for the two models in Fig. 5. As commented on in Ref. [88], for these choices of parameters both of these models give rise to a deficit in the CMB temperature power spectrum at $\ell \sim 20$–30, similar to what is observed.

C. Results

In Table I, we present the results of our multitracer analysis. For each model, we show the FoMr that captures how constraints on model parameters improve when the observable set is extended beyond the primary CMB temperature T. For those cells that correspond to a set including the remote fields R, we have included two values: the FoMr when the small scale CMB noise has beam size $\theta_{\rm FWHM}$ equal to 5 arcmin and 1 arcmin. This further emphasizes the dependence of the reconstruction signal to noise ratio on the instrumental noise of the high resolution CMB experiment.

The results displayed on Table I tell us a consistent story across the different models. The inclusion of the E mode polarization into the analysis of CMB anomalies

TABLE I. Figure of merit ratios for the anomaly models under study.

Model	Noise [μ-Karcmin]	FoMr(T,E)	FoMr(T,E,R)	FoMr(T,E,G)	FoMr(T,E,R,G)
Dipolar modulation	5.0	1.48	1.60–2.37	2.90	2.90–3.02
	1.0	1.48	1.87–2.67	2.90	2.93–3.13
	0.1	1.48	2.27–2.72	2.90	3.00–3.17
Exponential suppression	5.0	1.46	1.48–1.63	1.69	1.69–1.75
	1.0	1.46	1.55–1.70	1.69	1.72–1.81
	0.1	1.46	1.63–1.78	1.69	1.76–1.86
Broken power law	5.0	1.69	1.76–1.79	1.90	1.94–1.98
	1.0	1.69	1.78–1.83	1.90	1.97–1.99
	0.1	1.69	1.82–1.92	1.90	1.99–2.02
Cutoff	5.0	2.05	2.14–2.46	2.60	2.63–2.74
	1.0	2.05	2.27–2.63	2.60	2.68–2.82
	0.1	2.05	2.46–2.77	2.60	2.75–2.92
Step in inflaton potential	5.0	3.09	3.25–3.81	3.88	3.89–4.08
	1.0	3.09	3.50–4.07	3.88	3.98–4.24
	0.1	3.09	3.78–4.18	3.88	4.09–4.31

brings substantial constraining power, here represented by a FoMr ranging from 1.5 to 3.0. Beyond this, the following two questions are important to address: how do constraints improve if we add the remote dipole and quadrupole fields, and how does this improvement relate to what can be done by instead choosing galaxy clustering on large scales as the additional observable? We can see that depending on the noise conditions for the small scale CMB experiment, the remote fields compete with the large scale galaxy clustering in improving the FoMr beyond the (T, E) combination, with a tendency of the galaxies to be superior than the dipole and quadrupole except for very sensitive CMB experiments. However, the remote fields contain a significant amount of new information, as evidenced by the last column of Table I. Adding the dipole and quadrupole fields on top of (T, E, G) can increase the FoMr by $\sim$10%. Given that observations of the large scale polarization or galaxy clustering can be limited by different systematics and foregrounds than the high angular resolution measurements necessary for SZ tomography and vice versa,the remote dipole and quadrupole are an "extra handle" to work with when other tracers fall short, and which has prospects of becoming increasingly informative as detector technology keeps developing.

The FoMr gives us a general idea of how constraints improve for different data sets, but its also useful to look directly at parameter constraints (Appendix A) to see how helpful these combinations of observables can be in the task of determining the physical nature of the CMB anomalies. Keeping in mind that ultimately only a full likelihood analysis will reveal if departures of ΛCDM are favored by data, we can see that the full set of observables here considered can push marginal 1σ–3σ constraints to tighter ones. For the dipolar modulation model, constraints on the amplitude of modulation can be pushed from 3σ to 8σ and for the crossover scale constraints can be pushed from the 1σ to the 3σ level. For the generic suppression models, constraints on the characteristic scale of suppression can be pushed from the 1σ to 2σ level and in the case of the step model, the amplitude $\mathcal{A}_s$ of the step and the parameter x_s controlling its shape; see constraints jumping from marginality to above the 4σ level. These results indicate a much more optimistic possibility of studying the CMB anomalies beyond what the primary CMB temperature allows for. The reconstructed dipole and quadrupole will therefore form part of a set of observables that can provide stronger evidence to favor or rule out new early Universe physics.

V. CONCLUSIONS

Determining whether or not the observed large angular scale anomalies in the CMB are indications of physics beyond ΛCDM is a matter of great interest and intense debate. Faced with the obstacle imposed by cosmic variance on our study of the largest scales in the Universe, we are driven to analyze data sets that incorporate additional observables on top of the primary CMB temperature in order to favor or rule out the different hypotheses for the origin of the anomalies.

In this paper, we explored the constraining power on CMB anomalies models provided by a new set of observables: the remote CMB dipole and quadrupole fields. These fields, which correspond to the projected $\ell = 1, 2$ moments of the microwave sky as measured at different locations in the Universe, can be reconstructed using SZ tomography. The remote dipole and quadrupole

fields carry three-dimensional information about large scale fluctuations in the Universe, and a significant number of independent modes can in principle be reconstructed from next-generation CMB and galaxy surveys. This additional information is largely independent of the primary CMB and can therefore offer more statistical power for the analysis of physical models of large scale CMB anomalies.

Our methodology consisted of deriving forecasted constraints on a series of anomalies models using different combinations of observables probing the largest scales, including the primary CMB temperature (T), E-model polarization (E), galaxy clustering on large scales (G), and the remote dipole and quadrupole fields (R). The improvement on constraints relative to what is achievable with the primary CMB temperature serves as a measure of how informative additional observables can be, and this was expressed in terms of appropriate figure of merit ratios (FoMr); see Eq. (10). We assumed access to data on the full sky, with no systematics (aside from CMB instrumental noise, photometric redshift errors, and photometric calibration errors) or foregrounds, in each of our forecasts.

We considered a series of representative models for CMB anomalies, capturing departures from statistical isotropy and the standard inflationary ΛCDM primordial power spectrum. These modifications have been considered as possible explanations for the statistically marginal power asymmetry on the CMB sky, as well as features and lack of power in the temperature power spectrum on large angular scales. Based on our analysis, we can make a number of general statements about the utility of SZ tomography for addressing the possible physical nature of the CMB anomalies. As many previous analyses have shown [4–11], E-mode polarization has been identified as a powerful discriminator for physical models of CMB anomalies. We found that one can go beyond the (T, E) combination by adding the reconstructed remote dipole and quadrupole field, as it was expected due to their three-dimensional nature. A comparable amount of information can also be accessed using a more commonly considered three-dimensional probe: galaxy clustering on our past light cone. Because of this, we explored the ability of the remote fields to improve over the (T, E, G) constraints, finding that typically one can achieve higher FoMrs up to 10%, with better results for more sensitive CMB experiments. This means that there is new information on the large scale Universe that becomes available through SZ tomography. Overall, our results suggest that the remote dipole/quadrupole fields could play the role of an alternative and complementary probe of the CMB anomalies, affected by different systematics or foregrounds that make difficult a cosmic variance limited measurement of large scale E-mode polarization or galaxy clustering. SZ tomography also offers the possibility to systematically improve constraints on CMB anomaly models in the current era of rapidly evolving high-resolution, low-noise CMB experiments. All together, the observable set that we considered here was able to push several marginal parameter constraints on anomaly models to above the 3σ level and even higher. This indicates that next-generation CMB experiments and galaxy surveys will allow for an enhanced testing of the nature of the large scale CMB anomalies.

Our analysis has a number of shortcomings. First, our Fisher-based analysis is insensitive to the shape of the likelihood function, which can deviate significantly from a Gaussian for many of the models considered here. A future investigation could improve upon this by sampling the full likelihood function; however, given the size of the covariance matrix including all observables and the dimensionality of the parameter space, there will be computational challenges for doing so. Future analyses should also incorporate realistic foregrounds and systematics in the CMB and galaxy surveys and investigate their impact on the reconstruction of the remote dipole and quadrupole fields. In addition, the effects of masking should be taken into account, which will degrade the information available on the largest angular scales. Despite these limitations, our analysis highlights there is useful information on the physical nature of the observed CMB anomalies that is *in principle* accessible using SZ tomography. This provides a useful target for future analyses and observations.

ACKNOWLEDGMENTS

We would like to thank Dagoberto Contreras, James Mertens, and Moritz Münchmeyer for helpful discussions. This research was supported in part by Perimeter Institute for Theoretical Physics. Research at Perimeter Institute is supported by the Government of Canada through the Department of Innovation, Science and Economic Development Canada and by the Province of Ontario through the Ministry of Research, Innovation, and Science. M. C. J. was supported by the National Science and Engineering Research Council through a Discovery grant.

APPENDIX A: CONSTRAINTS ON MODEL PARAMETERS

We present here the constraints on model parameters derived using Fisher analysis of different combinations of primary CMB and remote dipole and quadrupole fields. We include the constraint using only the primary CMB temperature as well. Characteristic scale parameters k_c, k_b, and k_s are in units of Mpc^{-1}.

Dipolar modulation model.

Parameter	Noise [μ Karcmin]	$\sigma(T)$	$\sigma(T, E)$	$\sigma(T, E, R)$	$\sigma(T, E, G)$	σ(All)
$10^2 A := 7.00$	5.0	1.93	1.04	1.03–0.92	0.85	0.85–0.85
	1.0	1.93	1.04	0.98–0.87	0.85	0.84–0.83
	0.1	1.93	1.04	0.92–0.86	0.85	0.84–0.83
$10^3 k_c := 7.83$	5.0	6.36	4.50	4.40–3.46	2.76	2.76–2.73
	1.0	6.36	4.50	4.08–3.05	2.76	2.74–2.69
	0.1	6.36	4.50	3.58–2.97	2.76	2.73–2.67
$10\Delta \ln k := 5.00$	5.0	0.17	0.12	0.10–0.05	0.04	0.04–0.04
	1.0	0.17	0.12	0.08–0.04	0.04	0.04–0.03
	0.1	0.17	0.12	0.05–0.04	0.04	0.04–0.03

Exponential suppression model.

Parameter	Noise [μ Karcmin]	$\sigma(T)$	$\sigma(T, E)$	$\sigma(T, E, R)$	$\sigma(T, E, G)$	σ(All)
$10^4 k_c = 3.74$	5.0	3.05	2.33	2.23–2.21	2.04	2.03–1.94
	1.0	3.05	2.33	2.19–2.03	2.04	1.98–1.88
	0.1	3.05	2.33	2.09–1.90	2.04	1.92–1.80
$\lambda = 0.53$	5.0	0.25	0.18	0.17–0.15	0.15	0.14–0.14
	1.0	0.25	0.18	0.16–0.15	0.15	0.14–0.13
	0.1	0,25	0.18	0.15–0.14	0.15	0.14–0.13

Broken power law model.

Parameter	Noise [μ Karcmin]	$\sigma(T)$	$\sigma(T, E)$	$\sigma(T, E, R)$	$\sigma(T, E, G)$	σ(All)
$10^4 k_b = 5.26$	5.0	5.03	2.89	2.79–2.74	2.60	2.55–2.51
	1.0	5.03	2.89	2.75–2.68	2.60	2.52–2.47
	0.1	5.03	2.89	2.70–2.54	2.60	2.49–2.45
$\delta = 1.14$	5.0	2.85	1.59	1.50–1.47	1.36	1.32–1.29
	1.0	2.85	1.59	1.48–1.43	1.36	1.30–1.28
	0.1	2.85	1.59	1.44–1.34	1.36	1.28–1.26

Cutoff model.

Parameter	Noise [μ Karcmin]	$\sigma(T)$	$\sigma(T, E)$	$\sigma(T, E, R)$	$\sigma(T, E, G)$	σ(All)
$10^4 k_c = 3.63$	5.0	0.78	0.38	0.37–0.32	0.30	0.30–0.29
	1.0	0.78	0.38	0.34–0.30	0.30	0.29–0.28
	0.1	0.78	0.38	0.32–0.28	0.30	0.28–0.27

Step model.

Parameter	Noise [μ Karcmin]	$\sigma(T)$	$\sigma(T, E)$	$\sigma(T, E, R)$	$\sigma(T, E, G)$	σ(All)
$10\mathcal{A}_s = 3.74$	5.0	2.80	1.11	1.05–0.91	0.93	0.91–0.85
	1.0	2.80	1.11	0.97–0.85	0.93	0.88–0.81
	0.1	2.80	1.11	0.90–0.82	0.93	0.85–0.80
$10^4 k_s = 7.94$	5.0	0.72	0.18	0.17–0.14	0.14	0.14–0.13
	1.0	0.72	0.18	0.16–0.13	0.14	0.14–0.13
	0.1	0.72	0.18	0.14–0.13	0.14	0.13–0.13
$x_s = 1.41$	5.0	0.60	0.25	0.24–0.20	0.19	0.19–0.18
	1.0	0.60	0.25	0.22–0.18	0.19	0.19–0.17
	0.1	0.60	0.25	0.20–0.18	0.19	0.18–0.17

APPENDIX B: MODE COUPLING

The superhorizon modulating field $h(\vec{x})$ introduced in the spontaneous isotropy breaking mechanism here studied leads to couplings between different multipole moments. The modified primordial spectrum Eq. (15) is used to compute the covariance matrix, which differs from the ΛCDM covariance matrix by terms linear and quadratic in the modulation amplitude A,

$$
\begin{aligned}
C^{X,Y}_{\alpha\beta,\ell\ell',mm'} &= C^{X,Y,(\Lambda\mathrm{CDM})}_{\alpha\beta,\ell\ell',mm'} + C^{X,Y,(A)}_{\alpha\beta,\ell\ell',mm'} + C^{X,Y,(A^2)}_{\alpha\beta,\ell\ell',mm'} \\
C^{X,Y,(A)}_{\alpha\beta,\ell\ell',mm'} &= \delta_{mm'}\sqrt{\frac{4\pi}{3}}\frac{A}{i\chi_{\mathrm{dec}}}\int\frac{dkk^2}{(2\pi)^3}P_\psi(k)\Big[\Delta^{*X,\alpha}_\ell(k)\partial_k\Delta^{Y,\beta}_{\ell'}(k) - \partial_k\Delta^{*X,\alpha}_\ell(k)\Delta^{Y,\beta}_{\ell'}(k) \\
&\quad - \frac{2\Delta^{*X,\alpha}_\ell(k)\Delta^{Y,\beta}_{\ell'}(k)}{k}(\ell\delta_{l',l-1} - (\ell+1)\delta_{l',l+1})\Big]R^{1\ell'}_{\ell m} \\
C^{X,Y,(A^2)}_{\alpha\beta,\ell\ell',mm'} &= \delta_{mm'}\frac{4\pi}{3}\frac{A^2}{\chi^2_{\mathrm{dec}}}\int\frac{dkk^2}{(2\pi)^3}P_\psi(k)\sum_L R^{1L}_{\ell m}R^{1L}_{\ell' m}\Big[\partial_k\Delta^{*X,\alpha}_\ell(k)\partial_k\Delta^{*Y,\beta}_{\ell'}(k) \\
&\quad + \frac{\partial_k\Delta^{*X,\alpha}_\ell(k)\Delta^{Y,\beta}_{\ell'}(k)}{k}((1+\ell')\delta_{L,\ell'-1} - \ell'\delta_{L,\ell'+1}) + \frac{\Delta^{*X,\alpha}_\ell(k)\partial_k\Delta^{Y,\beta}_{\ell'}(k)}{k}((1+\ell)\delta_{L,\ell-1} - \ell\delta_{L,\ell+1}) \\
&\quad + \frac{\Delta^{*X,\alpha}_\ell(k)\Delta^{Y,\beta}_{\ell'}(k)}{k^2}((1+\ell)^2\delta_{L,\ell-1}\delta_{\ell',\ell} + \ell^2\delta_{L,\ell+1}\delta_{\ell',\ell} \\
&\quad - (1+\ell)(\ell-2)\delta_{L,\ell-1}\delta_{\ell',\ell-2} - \ell(\ell+3)\delta_{L,\ell+1}\delta_{\ell',\ell+2})\Big],
\end{aligned}
$$

where the couplings $R^{\ell_1\ell_2}_{\ell m}$ are defined through the 3-j Wigner symbols,

$$
R^{\ell_1\ell_2}_{\ell m} = (-1)^m\sqrt{\frac{(2\ell+1)(2\ell_1+1)(2\ell_2+1)}{4\pi}}\begin{pmatrix}\ell_1 & \ell_2 & \ell\\ 0 & 0 & 0\end{pmatrix}\begin{pmatrix}\ell_1 & \ell_2 & \ell\\ 0 & m & -m\end{pmatrix}. \tag{B1}
$$

The term linear in A induces couplings between multipoles ℓ and $\ell\pm1$, while the quadratic term adds couplings between ℓ and $\ell\pm2$ as well as the same multipole corrections to the covariance matrix. For the particular case of temperature transfer functions in the Sachs-Wolfe approximation, i.e., $\Delta^T_\ell(k)\propto j_\ell(k\chi_{dec})$, the above expressions can be reduced to those presented in [4,73] using appropriate recursion relations for the derivatives of the spherical Bessel functions. A similar approach to compute the multipole couplings in terms of derivatives of the transfer functions was taken in Ref. [90], although the assumptions on the modulation of the primordial spectrum are not the same as ours, and the $\mathcal{O}(A^2)$ term was not computed.

[1] C. L. Bennett *et al.* (WMAP Collaboration), Astrophys. J. **583**, 1 (2003).
[2] J. A. Tauber, N. Mandolesi, J. Puget *et al.*, Astron. Astrophys. **520**, A1 (2010).
[3] D. J. Schwarz, C. J. Copi, D. Huterer, and G. D. Starkman, Classical Quantum Gravity **33**, 184001 (2016).
[4] C. Dvorkin, H. V. Peiris, and W. Hu, Phys. Rev. D **77**, 063008 (2008).
[5] C. J. Copi, D. Huterer, D. J. Schwarz, and G. D. Starkman, Mon. Not. R. Astron. Soc. **434**, 3590 (2013).
[6] A. Yoho, S. Aiola, C. J. Copi, A. Kosowsky, and G. D. Starkman, Phys. Rev. D **91**, 123504 (2015).
[7] M. O'Dwyer, C. J. Copi, L. Knox, and G. D. Starkman, Mon. Not. R. Astron. Soc. **470**, 372 (2017).
[8] E. F. Bunn, Q. Xue, and H. Zheng, Phys. Rev. D **94**, 103512 (2016).
[9] D. Contreras, J. P. Zibin, D. Scott, A. J. Banday, and K. M. Górski, Phys. Rev. D **96**, 123522 (2017).
[10] G. Obied, C. Dvorkin, C. Heinrich, W. Hu, and V. Miranda, Phys. Rev. D **98**, 043518 (2018).

[11] M. Billi, A. Gruppuso, N. Mandolesi, L. Moscardini, and P. Natoli, Phys. Dark Universe **26**, 100327 (2019).
[12] A. Yoho, C. J. Copi, G. D. Starkman, and A. Kosowsky, Mon. Not. R. Astron. Soc. **442**, 2392 (2014).
[13] J. P. Zibin and D. Contreras, Phys. Rev. D **95**, 063011 (2017).
[14] J. Muir and D. Huterer, Phys. Rev. D **94**, 043503 (2016).
[15] C. J. Copi, M. O'Dwyer, and G. D. Starkman, Mon. Not. R. Astron. Soc. **463**, 3305 (2016).
[16] S. Foreman, P. D. Meerburg, J. Meyers, and A. van Engelen, Phys. Rev. D **99**, 083506 (2019).
[17] X. Chen, C. Dvorkin, Z. Huang, M. H. Namjoo, and L. Verde, J. Cosmol. Astropart. Phys. 11 (2016) 014.
[18] X. Chen, P. D. Meerburg, and M. Münchmeyer, J. Cosmol. Astropart. Phys. 09 (2016) 023.
[19] M. Ballardini, F. Finelli, R. Maartens, and L. Moscardini, J. Cosmol. Astropart. Phys. 04 (2018) 044.
[20] G. A. Palma, D. Sapone, and S. Sypsas, J. Cosmol. Astropart. Phys. 06 (2018) 004.
[21] N. Aghanim *et al.* (Planck Collaboration), arXiv:1807.06209.
[22] J. Aguirre *et al.* (Simons Observatory), J. Cosmol. Astropart. Phys. 02 (2019) 056.
[23] K. N. Abazajian *et al.* (CMB-S4 Collaboration), arXiv:1610.02743.
[24] P. A. Abell *et al.* (LSST Science and LSST Project), arXiv:0912.0201.
[25] R. Laureijs *et al.*, arXiv:1110.3193.
[26] O. Doré *et al.*, arXiv:1412.4872.
[27] J. R. Shaw, K. Sigurdson, U.-L. Pen, A. Stebbins, and M. Sitwell, Astrophys. J. **781**, 57 (2014).
[28] L. B. Newburgh *et al.*, Proc. SPIE Int. Soc. Opt. Eng. **9906**, 99065X (2016).
[29] R. Ansari *et al.* (Cosmic Visions 21 cm), arXiv:1810.09572.
[30] F. Elsner, B. Leistedt, and H. V. Peiris, Mon. Not. R. Astron. Soc. **456**, 2095 (2016).
[31] R. A. Sunyaev and I. B. Zeldovich, Mon. Not. R. Astron. Soc. **190**, 413 (1980).
[32] S. Ho, S. Dedeo, and D. Spergel, arXiv:0903.2845.
[33] J. Shao, P. Zhang, W. Lin, Y. Jing, and J. Pan, Mon. Not. R. Astron. Soc. **413**, 628 (2011).
[34] P. Zhang and A. Stebbins, Phys. Rev. Lett. **107**, 041301 (2011).
[35] P. Zhang and U.-L. Pen, Astrophys. J. **549**, 18 (2001).
[36] D. Munshi, I. T. Iliev, K. L. Dixon, and P. Coles, Mon. Not. R. Astron. Soc. **463**, 2425 (2016).
[37] E. Schaan *et al.* (ACTPol Collaboration), Phys. Rev. D **93**, 082002 (2016).
[38] S. Ferraro, J. C. Hill, N. Battaglia, J. Liu, and D. N. Spergel, Phys. Rev. D **94**, 123526 (2016).
[39] J. C. Hill, S. Ferraro, N. Battaglia, J. Liu, and D. N. Spergel, Phys. Rev. Lett. **117**, 051301 (2016).
[40] P. Zhang, Mon. Not. R. Astron. Soc. **407**, L36 (2010).
[41] P. Zhang and M. C. Johnson, J. Cosmol. Astropart. Phys. 06 (2015) 046.
[42] A. Terrana, M.-J. Harris, and M. C. Johnson, J. Cosmol. Astropart. Phys. 02 (2017) 040.
[43] A.-S. Deutsch, E. Dimastrogiovanni, M. C. Johnson, M. Münchmeyer, and A. Terrana, Phys. Rev. D **98**, 123501 (2018).
[44] K. M. Smith, M. S. Madhavacheril, M. Münchmeyer, S. Ferraro, U. Giri, and M. C. Johnson, arXiv:1810.13423.
[45] M. Münchmeyer, M. S. Madhavacheril, S. Ferraro, M. C. Johnson, and K. M. Smith, Phys. Rev. D **100**, 083508 (2019).
[46] N. Sehgal *et al.*, arXiv:1903.03263.
[47] M. Kamionkowski and A. Loeb, Phys. Rev. D **56**, 4511 (1997).
[48] E. F. Bunn, Phys. Rev. D **73**, 123517 (2006).
[49] J. Portsmouth, Phys. Rev. D **70**, 063504 (2004).
[50] E. Alizadeh and C. M. Hirata, Phys. Rev. D **85**, 123540 (2012).
[51] A. Hall and A. Challinor, Phys. Rev. D **90**, 063518 (2014).
[52] A.-S. Deutsch, M. C. Johnson, M. Münchmeyer, and A. Terrana, arXiv:1705.08907.
[53] T. Louis, E. F. Bunn, B. Wandelt, and J. Silk, Phys. Rev. D **96**, 123509 (2017).
[54] J. Meyers, P. D. Meerburg, A. van Engelen, and N. Battaglia, Phys. Rev. D **97**, 103505 (2018).
[55] A.-S. Deutsch, E. Dimastrogiovanni, M. Fasiello, M. C. Johnson, and M. Münchmeyer, Phys. Rev. D **100**, 083538 (2019).
[56] J. I. Cayuso, M. C. Johnson, and J. B. Mertens, Phys. Rev. D **98**, 063502 (2018).
[57] N. Seto and E. Pierpaoli, Phys. Rev. Lett. **95**, 101302 (2005).
[58] N. Battaglia, J. Cosmol. Astropart. Phys. 08 (2016) 058.
[59] M. S. Madhavacheril, N. Battaglia, K. M. Smith, and J. L. Sievers, Phys. Rev. D **100**, 103532 (2019).
[60] A. Terrana, M.-J. Harris, and M. C. Johnson, J. Cosmol. Astropart. Phys. 02 (2017) 040.
[61] A.-S. Deutsch, M. C. Johnson, M. Münchmeyer, and A. Terrana, J. Cosmol. Astropart. Phys. 04 (2018) 034.
[62] P. D. Meerburg, J. Meyers, and A. van Engelen, Phys. Rev. D **96**, 083519 (2017).
[63] A. Lewis and A. Challinor, Phys. Rep. **429**, 1 (2006).
[64] J. P. Zibin and D. Scott, Phys. Rev. D **78**, 123529 (2008).
[65] S. Yasini and E. Pierpaoli, Phys. Rev. D **96**, 103502 (2017).
[66] R. Trotta, Mon. Not. R. Astron. Soc. **378**, 819 (2007).
[67] A. Albrecht, L. Amendola, G. Bernstein, D. Clowe, D. Eisenstein, L. Guzzo, C. Hirata, D. Huterer, R. Kirshner, E. Kolb, and R. Nichol, arXiv:0901.0721.
[68] A. Lewis and A. Challinor, Astrophysics Source Code Library, 02026 (2011), https://ui.adsabs.harvard.edu/abs/2011ascl.soft02026L/abstract.
[69] D. Contreras, M. C. Johnson, and J. B. Mertens, J. Cosmol. Astropart. Phys. 10 (2019) 024.
[70] J. Muir and D. Huterer, Phys. Rev. D **94**, 043503 (2016).
[71] N. Weaverdyck, J. Muir, and D. Huterer, Phys. Rev. D **97**, 043515 (2018).
[72] Planck Collaboration, Astron. Astrophys. **594**, A16 (2016).
[73] C. Gordon, W. Hu, D. Huterer, and T. Crawford, Phys. Rev. D **72**, 103002 (2005).
[74] A. L. Erickcek, M. Kamionkowski, and S. M. Carroll, Phys. Rev. D **78**, 123520 (2008).
[75] A. R. Liddle and M. Cortês, Phys. Rev. Lett. **111**, 111302 (2013).
[76] T. Kobayashi, M. Cortês, and A. R. Liddle, J. Cosmol. Astropart. Phys. 05 (2015) 029.

[77] S. Adhikari, S. Shandera, and A. L. Erickcek, Phys. Rev. D **93**, 023524 (2016).
[78] D. Contreras, J. Hutchinson, A. Moss, D. Scott, and J. P. Zibin, Phys. Rev. D **97**, 063504 (2018).
[79] C. M. Hirata, J. Cosmol. Astropart. Phys. 09 (2009) 011.
[80] A. D. Linde, Phys. Rev. D **59**, 023503 (1998).
[81] D. Yamauchi, A. Linde, A. Naruko, M. Sasaki, and T. Tanaka, Phys. Rev. D **84**, 043513 (2011).
[82] C. R. Contaldi, M. Peloso, L. Kofman, and A. Linde, J. Cosmol. Astropart. Phys. 07 (2003) 002.
[83] X. Chen, R. Easther, and E. A. Lim, J. Cosmol. Astropart. Phys. 06 (2007) 023.
[84] E. Silverstein and D. Tong, Phys. Rev. D **70**, 103505 (2004).
[85] J. A. Adams, B. Cresswell, and R. Easther, Phys. Rev. D **64**, 123514 (2001).
[86] A. Achucarro, J.-O. Gong, S. Hardeman, G. A. Palma, and S. P. Patil, J. Cosmol. Astropart. Phys. 01 (2011) 030.
[87] R. Bean, X. Chen, G. Hailu, S. H. H. Tye, and J. Xu, J. Cosmol. Astropart. Phys. 03 (2008) 026.
[88] P. Collaboration, Astron. Astrophys. **594**, A20 (2016).
[89] V. Miranda and W. Hu, Phys. Rev. D **89**, 083529 (2014).
[90] G. Kashyap, P. Jain, P. K. Rath, R. Kothari, and S. Ghosh, Mon. Not. R. Astron. Soc. **460**, 1577 (2016).